JOURNAL OF SPACECRAFT AND ROCKETS
Vol. 37, No. 2, March–April 2000

Electromagnetic and Aeromechanical Analysis of Sabot Discard for Railgun Projectiles

Alexander E. Zielinski* and Paul Weinacht†
U.S. Army Research Laboratory, Aberdeen Proving Ground, Maryland 21005-5066
and
John Bennett‡
U.S. Army Tank-Automotive and Armaments Command–Armaments Research, Development, and Engineering Center, Picatinny Arsenal, New Jersey 07801

Experimental and engineering modeling techniques were applied to examine the role that electromagnetics plays during the sabot discard process in a solid-armature railgun. Current and magnetic field diffusion in the conducting armature and sabot produce residual forces that tend to clamp the sabot petals during in-bore acceleration and after launch. The effect of this force on sabot discard was investigated. The experimental portion of this work used the measured downrange magnetic fields to quantify the effect on subprojectile performance. The time rate of change of launcher and switch currents and launcher voltages were measured. In addition, the time rate of change of the armature magnetic field was measured downrange from the launcher. Electrical parameters that characterize the magnetic fields were used to calculate the residual current flowing in the armature after exit. An engineering model that includes both aeromechanical and electromagnetic forces was developed to predict the sabot discard process. The model for the magnetic clamping force used the inferred current from the magnetic fields measured downrange. The results from the sabot discard analysis are in good agreement with the measured sabot trajectory data, particularly when the sabot petals are in close proximity. The analysis shows that the aerodynamic moment acting on the sabot is relatively small following launch, and small magnetic clamping forces could delay sabot separation.

Nomenclature

A_{pocket} = horizontal area of sabot petal pocket
a, b = downrange and transverse current loop dimensions, respectively
C_{m_α} = slope of the pitching moment coefficient with angle of attack
d = downrange distance from muzzle
$\mathrm{d}\boldsymbol{l}'$ = incremental arc-length vector along current loop
F_{aero} = sabot petal lifting force
F_{EM} = electromagnetic clamping force
F_{pocket} = sabot petal pocket force
$F_{x\text{-react}}$ = sabot petal reaction force in horizontal direction
$F_{z\text{-react}}$ = sabot petal reaction force in vertical direction
$\boldsymbol{H}$ = magnetic field vector
H_x = downrange component of magnetic field
H_y = orthogonal component of magnetic field
I = local inferred loop current in armature
I_o = average inferred loop current at muzzle exit
I_t = projectile transverse moment of inertia
l_{aero} = moment arm of sabot petal lifting force
l_{EM} = moment arm of electromagnetic clamping force
l_{pocket} = moment arm of sabot petal pocket force
M_∞ = freestream Mach number
m = projectile mass
P_{t_2} = stagnation pressure behind normal shock wave
P_2 = static pressure behind normal shock wave
P_∞ = freestream static pressure
p = separation distance between current loops in adjacent sabot petals
$\boldsymbol{r}$ = local position vector
$\boldsymbol{r}'$ = position vector along current loop
S = planform area of sabot petal
t = time
X = downrange distance between the sensor and the armature
x, z = horizontal and vertical displacements of sabot petals relative to projectile the body
γ = ratio of specific heats
θ = liftoff angle of sabot petal
μ_o = free-space permeability
τ = time constant associated with loop current

Superscript

$(\ddot{})$ = second derivative with respect to time

Received 3 March 1999; revision received 16 October 1999; accepted for publication 18 October 1999. This material is declared a work of the U.S. Government and is not subject to copyright protection in the United States.
*Electrical Engineer. Member AIAA.
†Aerospace Engineer. Associate Fellow AIAA.
‡Research Physicist.

Introduction

DELAYED sabot discard can significantly affect subprojectile accuracy and dispersion, resulting in marginal weapon system effectiveness. This paper addresses the issue of coupled electrodynamics and aeromechanical effects for sabot discard of direct fire, kinetic energy penetrators launched from electromagnetic (EM) railguns.

The impetus for this work originated in previous computations for the current and heat transport in the armature.[1] While residing in-bore, the transport current is conducted through the armature, which is in series with the rails. Magnetic energy, determined by the transport current and subsequent diffusion, is stored in the armature. A substantial amount of magnetic field is trapped in the armature conductor at the time of projectile exit. Upon exit, the transport current is disengaged from the armature, and an induced current decays in the armature.

The residual current and field after exit are oriented in the armature conductor so that the resultant force restrains the armature halves from separating in flight.[2] Additionally, the same electromagnetically generated force suspected of delaying sabot separation is also present throughout the in-bore acceleration. If this force is large enough, the armature halves could be mechanically swaged and locked to the subprojectile body during acceleration, thereby impeding the discard process. An illustration depicting the current flow in the armature during acceleration and after exit is shown in Fig. 1.

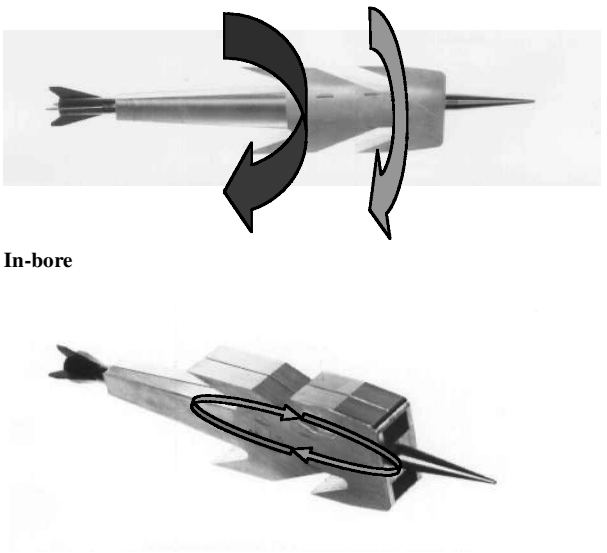

In-bore

Downrange

Fig. 1 Illustration of armature current while in-bore (top) and after exit (bottom).

In prior experimental work, the motion of the armature halves exhibited a suspicious delay in separation as a function of downrange distance.[3] The unique shape of the armature offered an explanation for the retarded discard. However, it was felt that the presence of an EM effect could, in fact, significantly alter the design of future-bore cross sections, pulsed power supplies, and armatures. In more recent work,[4] experiments to evaluate the launch dynamics were conducted in which the amount of peak magnetic field (i.e., residual current) was varied. Relatively minor changes in the launch dynamics were observed.

An experimental approach was used to evaluate the effect of railgun electrodynamics on sabot discard. The downrange component of the magnetic field produced by circulating currents within the armature during sabot discard was investigated. In the experiment the rail current in the armature was forced to zero before exit. However, diffusion of the magnetic field during the in-bore acceleration prevented the field from being zero at exit. The field persists in the armature conductor after exit. The amount of trapped field is proportional to the peak launcher current and will decay during sabot discard.

A simple aeromechanical model that describes the trajectory of the sabot petals was developed. The model is based on simple compressible flow theories, which approximate the complicated aerodynamic behavior of the sabot petals. The aeromechanical and electrodynamic models are specifically tailored to the present experimental configuration. The model qualitatively reproduces the sabot petal trajectories and allows the relative influences of the aerodynamic and EM forces and moments to be assessed.

Experiment

Testing took place in the EM launch facility at the transonic experimental facility, Aberdeen Proving Ground, Maryland. The facility consists of eight 200-kJ capacitor banks, a launcher, and a 222-m flight range. The capacitor output current produces a sinusoidal rise to current peak and an exponential decay thereafter. The rise to peak current takes roughly 0.46 ms, and the time constant for the exponential decay is roughly 3 ms. The short circuit admittance is nominally 120 and 84 kA/kV with the railgun launcher as the electrical load.

The launch package (armature and subprojectile) used in the current study is shown in Fig. 2. The launch package has been adapted from the launch package used in the cannon caliber electromagnetic gun (CCEMG) accuracy survey,[3] although several important differences exist. In the current study the subprojectile was fabricated from steel instead of tungsten and weighs 42 gm. The lower weight subprojectile can be more easily displaced and the launch disturbances more easily observed. Aerodynamic stabilization was

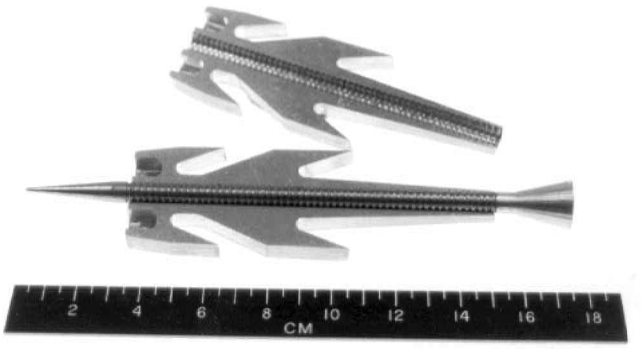

Fig. 2 Photograph of launch package.

provided by a 14-deg aluminum flare that provides enhanced stability and was easier to manufacture than the four-bladed fin used on the CCEMG subprojectile. The modification results in a very low-cost, low-risk round.

The general shape of the CCEMG armature has been adapted. The discarded portion of the launch package is a midriding sabot with an integrated tandem contact armature. The two sets of armature contacts are used to minimize the disturbances on the subprojectile caused by in-bore loads and to distribute the accelerating forces in the forward section of the sabot. Normally, pins that allow the armature to pivot off the subprojectile during discard were not used. Also, the scoop that generates pressure during the transitional ballistic phase had a flat base and had roughly twice the volume as the CCEMG design to enhance sabot liftoff. The armature was machined from 6061-T6 aluminum, and each petal weighs 49 g.

The launcher developed under the CCEMG program was selected for this experimental investigation.[5] The bore is rectangular, having dimensions of 17 × 40 mm. It is a 2.25-m-long railgun that incorporates a conducting loop which traverses the length of the launcher. This loop provides for increased propulsive force from the augmented in-bore magnetic field. An explosively activated muzzle switch (EAMS) was used to divert the armature current ahead of the armature. The EAMS is connected across the rails near the muzzle. When the switch is closed, the current is diverted from the armature to the switch, according to the dynamic impedance of the inductively coupled railgun and switch circuits. A lumped parameter, equivalent circuit model similar to that used in previous work[6] was used to plan the test matrix. Given the EAMS performance, launch package mass, and test objectives, the determination was made that a launch velocity of 1100 m/s could be readily achieved. An initial charge voltage of 5.2 kV was selected to produce the current profile. Specifying a velocity greater than 1100 m/s results in muzzle switch currents greater than 350 kA, which can significantly damage the connections to the EAMS.

The electrical performance of the launcher was monitored through measurements of the time rate of change in launcher and EAMS currents and the breech and muzzle voltages. In previous work, an analysis of the measured breech and muzzle voltage and its relation to the armature function was documented.[6] The measured breech and muzzle voltages are indicative of the electrical performance of the armature contacts. The voltages associated with the augmented launcher are much larger than those measured in a regular (i.e., single turn) railgun, and the additional voltage contributions are attributable to the augmenting turn. The muzzle voltage waveform is consistent with previous analysis[6] in that little or no current was carried in the front contact. Also, the breech voltage waveform is consistent with a rear contact that has transitioned from a solid to a plasma state. Although the electrical aspects of a transitioned armature contact are deleterious to the system efficiency, there are no differences in the electrical behavior of the armature contacts for each test.

A typical armature current pulse, derived from the measured launcher and EAMS currents, is plotted in Fig. 3. The launcher (and armature) current rises to a peak of 450 kA in 0.46 ms and then exponentially decays. At 2.38 ms the muzzle switch is initiated (the armature has traveled approximately 1.4 m), and the transfer of current in the armature to the rails is completed 0.6 ms later.

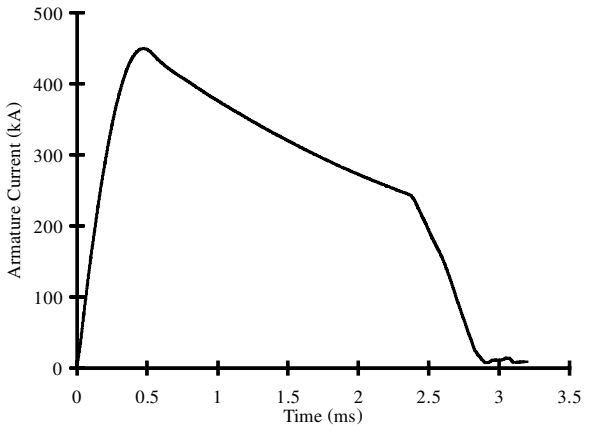

Fig. 3 Armature current pulse.

Previous work has shown some anomalies in the sabot discard and free-flight performance with regard to the mechanical interference between the subprojectile and sabot.[7] The interference was never quantitatively measured. Although no design guidelines exist relative to the dimensional tolerances required for satisfactory armature discard, the mechanical interference between the armature halves and the subprojectile has been assessed by measuring the torque required to turn the subprojectile while it is clamped in the armature. A compression force of roughly 29 kN (6600 lb) was applied to the launch package. The average torque required to turn the subprojectile was 1.7 N-m (15 in.-lb). Although there was some variation in the measured torque between the tested launch packages, there were no statistically significant differences in the measured torque values. In prior work the CCEMG integrated launch packages were fabricated so that the subprojectile required roughly 2.8 N-m (25 in.-lb). Therefore, mechanical interference is not expected to alter the conclusions from the test results.

The launch velocity was measured using the image recorded by the smear camera located 4.55 m downrange. The average velocity for the group of launch packages was 1097 m/s, ±72 m/s.

Measurements and Analysis

Experimental Data

A number of measurements were made on the launch package in order to assess sabot discard. In this section the techniques and measurements are explained in detail. Downrange instrumentation included flash x rays at 2.38 m, a smear camera at 4.55 m, and yaw cards at 6, 7, and 8 m. Additionally, an array of air-core coils was mounted within 0.5 m of the muzzle to measure the time rate of change in the downrange component of the armature magnetic field (dH_x/dt).

Because of the large quantity of data gathered, it is not reasonable to present all of the data for each shot. Also, rather than analyze the time history of each waveform in detail, significant data that readily characterize the waveform or ballistic process have been extracted and averaged.

The free-flight performance of the subprojectile, for determining the relative sabot discard disturbance, was assessed by measuring the angular motion of the round using a series of three yaw cards placed along the flight path of the projectile. The measurement of the free-flight dynamic response allows the quantitative assessment of the aerodynamic performance of the sabot and projectile and the launch disturbances that drive the free-flight motion. The pitch and yaw angles of the subprojectile were determined from the imprint produced by the impact of the subprojectile on each of the yaw cards. Computational fluid dynamics techniques, along with the measured physical properties, were used to determine the aerodynamic coefficients and pitching frequency of the subprojectile. The parabolized Navier–Stokes technique of Schiff and Steger,[8] which solves the thin-layer Navier–Stokes equations, was applied to compute the viscous flowfield about the projectile. This technique had been successfully applied to analyze the aerodynamic performance of the CCEMG subprojectile.[3] The aerodynamic predictions yielded a pitching moment coefficient C_{m_α} of −46 at the nominal launch velocity of 1100 m/s.

The angular motion of the subprojectile was fit to the equations of motion for a rolling symmetric missile,[9] using the measured pitch and yaw angles from the yaw cards and the predicted pitching moment coefficient. The reductions used here were obtained by assuming zero roll rate and no pitch damping. The data-fitting technique is similar to that used in the earlier investigation[3] except, in this study, the frequency of the pitching motion is obtained from the predicted pitching moment coefficient rather than from the measured motion. The yaw cards, x rays, and smear photographs confirm that the round is indeed in free flight by 5 m. The fitted maximum pitch and yaw angles are used to characterize the maximum and minimum angle of attack (AoA).

The amount of sabot discard disturbance can be inferred by considering the ratio of the minimum AoA to the maximum AoA of the subprojectile. When sabot discard disturbances are not present and the pitch and yaw are produced purely by in-bore disturbances, the transverse angular motion of a slowly rolling projectile should be nearly planar, and the minimum AoA should be zero. Disturbances generated during the sabot discard process can act perpendicularly to the plane of yaw generated by the in-bore disturbances generating a nonplanar yawing motion when the subprojectile nose traverses an elliptical path. In this case, the minimum yaw is greater than zero. Values greater than 20% generally indicate a fair amount of disturbance. The sabot disturbance can act in the same plane as the in-bore disturbance, producing zero minimum yaw. The ratio of minimum yaw to maximum yaw is only a relative indicator of the sabot disturbance.

The minimum yaw is roughly 15% of the maximum yaw for all of the tests. The average maximum AoA is 20 deg. The small magnitude of the minimum yaw relative to the maximum yaw indicates that the free-flight angles are primarily the result of rates generated at the launcher. Additional tests with a modified front contact produced an average AoA of about 5 deg with no change in the initiation of sabot discard.[4] In the results presented here, the sabot discard process is not likely to be a significant contributor to the free-flight yaw.

The measurement of dH_x/dt is made by using an air-core coil (i.e., sensor). Each sensor (eight total) is wound with 22 turns of No. 32 gauge wire on a 12-mm-diam form. The sensors are calibrated in a transverse EM wave cell. The sensors are subjected to a known value of continuous (i.e., ac) magnetic field as a function of frequency. The calibration factor converts the sensor output voltage to dH_x/dt. Subsequent numerical integration yields the downrange component of the magnetic field (H_x) in amperes/meter. The sensor array is placed 64 mm off the line of fire. The first coil was 150 mm from the muzzle end of the rails, and all of the coils were spaced with 50 mm between their centers. An illustration of the field measurement experimental arrangement is shown in Fig. 4.

Three sensors were used routinely to measure the magnetic field as the armature begins to discard. They are located at 150, 350, and 500 mm from the muzzle end of the rail. An example of the magnetic fields from the measured dH_x/dt data is shown in Fig. 5. If a loop of constant current in the rail plane of the armature is assumed, then the behavior can be described as follows. When the armature approaches the coil, the magnetic field begins to rise. The field is at a maximum when the current in the front portion of the armature is closest to the coil. When the centroid of the current loop is over the center of the

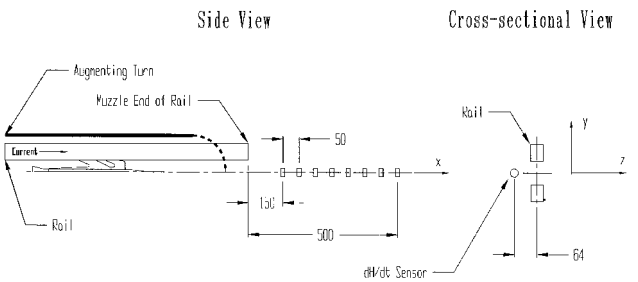

Fig. 4 Illustration of field measurement setup.

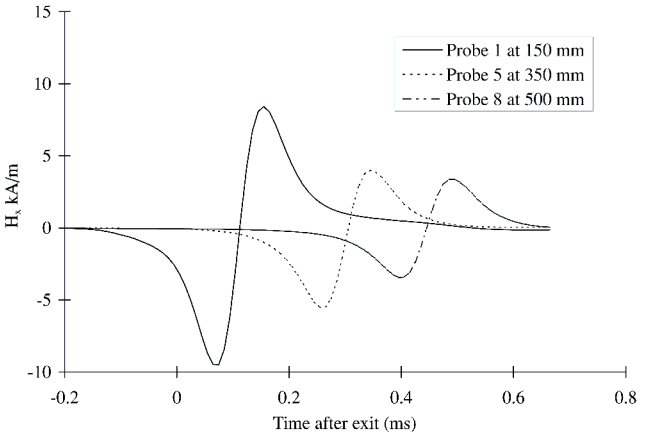

Fig. 5 Downrange magnetic fields for shot 28.

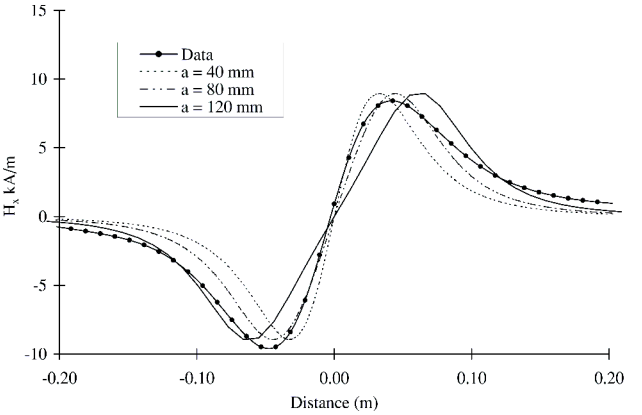

Fig. 6 Calculated and measured magnetic fields for various values of a.

coil, it produces a net axial component of the magnetic field of zero. Finally, as the armature proceeds downrange, the magnitude of the field begins to increase, reaching a maximum when the rear of the current loop is over the coil. The field now is opposite in direction to the field produced at the front of the current loop because the current is now in the opposite direction. The analysis using the zero crossings for the measured H_x data (1065 m/s, ±51 m/s) is in very good agreement with the velocity obtained from the data from the smear camera.

A straight-line fit was used to characterize the essential features of the magnetic field data. Selecting a straight-line fit aids in defining the axes intercepts. The positive and negative peak values of the field from each sensor were extrapolated to muzzle exit, and the average value is 13 kA/m. Similarly, an average distance where the field extrapolates to zero is found to be 0.73 m. If the magnetic field is assumed to decay exponentially as a function of time after the armature exits the launcher, the average time constant for the decay (i.e., the time it takes for the field at the muzzle to decay to 36% of its peak value) is calculated to be 0.35 ms.

A filamentary current flowing in the armature, defined by loop dimensions a and b, can be inferred from the measured magnetic field. The dimension a is in the direction of flight, and b is transverse to the downrange motion. The field can be derived from Ampere's law:

$$\boldsymbol{H} = \frac{I}{4\pi} \oint \frac{\mathrm{d}\boldsymbol{l}' \times (\boldsymbol{r} - \boldsymbol{r}')}{|\boldsymbol{r} - \boldsymbol{r}'|^3} \tag{1}$$

For the downrange component of the magnetic field H_x, the integral can be expanded as

$$H_x = \frac{I}{4\pi} \left\{ \int_{b/2}^{-b/2} \frac{-z\,\mathrm{d}y'}{\left[X_m + (y - y')^2 + z^2\right]^{\frac{3}{2}}} + \int_{-b/2}^{b/2} \frac{-z\,\mathrm{d}y'}{\left[X_p + (y - y')^2 + z^2\right]^{\frac{3}{2}}} \right\} \tag{2}$$

The resultant expression used to infer the current from the measured H_x data is

$$H_x = (Ibd/4\pi)\left[1\Big| \left(X_m + d^2\right)\sqrt{X_m + D} - 1\Big| \left(X_p + d^2\right)\sqrt{X_p + D}\right] \tag{3}$$

where the following relations apply: $X_m = (X - a/2)^2$, $X_p = (X + a/2)^2$, and $D = d^2 + b^2/4$. The variable X is a function of time and is the downrange displacement between the sensor and the armature, and d is the downrange displacement of the armature from the launcher muzzle. A similar expression can be derived for the orthogonal component of the magnetic field H_y using the preceding procedure.

The equation for the field is solved in terms of the current I, using the measured H_x. The assumption is made that the velocity is constant during the passage of the armature with respect to the sensor array and is determined from the zero crossings in the H_x data. Also, the zero crossing of the field data is assumed to be when the centroid of the current loop is coincidental with the probe location. In this manner the H_x data are synchronized at the downrange location of each probe, and the currents are evaluated fore and aft of the zero crossing.

The expression for H_x is used to estimate the downrange dimension of the current loop a. Certainly, maximum dimensions correspond to the physical attributes of the armature, namely $a = 120$ mm and $b = 40$ mm. By varying a and scaling the peak calculated magnetic field to the peak measured magnetic field, the general shape of H_x can be attained. Using the maximum value for b, the (scaled) calculated magnetic fields for $a = 40$, 80, and 120 mm are compared to the measured data in Fig. 6. Clearly, 40 and 120 mm are not effective at replicating the measured wave shape. A more rigorous approach yields a minimum error between the calculated and measured data for $a = 90$ mm. This value also corresponds very well to an analysis that uses the peak-to-peak spacing of the measured magnetic fields and the free-flight velocity. Also, the measured magnetic field data are not symmetrical about the zero crossing. The lack of symmetry in the measured magnetic field data suggests that the current flowing in the armature is not symmetrical, contrary to the assumptions in the preceding analytical development. From the data, it appears that slightly more current is flowing aft of the center of the loop. This result is expected because the rear portion of the armature is exposed to and conducts most of the field and current.

The dimension transverse to the armature motion b is inversely proportional to the measured field. Hence, selecting b equal to half of its maximum value results in an inferred current that is twice as large. Previous calculations indicate that most of the transport current is carried in the midsection of the armature.[1] Therefore, the width of this section ($b = 15$ mm) is used to complete the description of the current loop.

When the armature is far from the sensing coil, very little magnetic field is measured. Hence, measurement errors dominate this portion of the data. When the armature is located near the sensor, very large fields are present. However, the data are no longer appropriate for the assumed filament model carrying a uniform current. Therefore, the inferred current has limits, based on the data that correspond to the measurement error (i.e., 10% of the peak H_x or 1 kA/m) and the spatial location of the armature (i.e., $X > a$). There is also some error in assessing the location of the center of the loop relative to the probe location. Although the velocity obtained from the smear camera is in excellent agreement with the velocity obtained from the zero crossings of H_x, a small error in X calculated from the velocity can change the inferred current by an appreciable amount. For example, a change of 10 mm in the location of the center of the loop with respect to the sensor location results in approximately a 20-kA increase in the inferred current. Fortunately, the maximum error, as determined by the recorded data and the velocity of the launch package, is 10 mm.

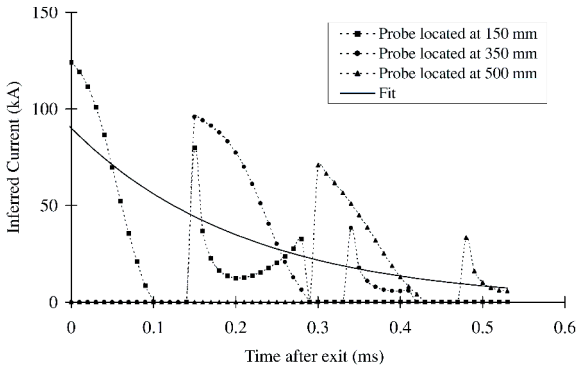

Fig. 7 Inferred current for shot 28.

A plot of the inferred current as a function of time for shot 28 is shown in Fig. 7. Close to the exit the current is on the order of 125 kA. Despite the fact that the transport current was zero in the launcher and armature at exit, some amount of field remains trapped in the conductor after being subjected to a peak in-bore current of 450 kA and 3 ms in duration. This residual field produces a 125-kA peak current that circulates in the conductor. As expected, the armature travels downrange, and the current decays. Also, during the flight, the field produced by the armature is sensed simultaneously by two adjacent probes. For example, when the armature has traveled 0.20 ms downrange, the field strength is sufficient so that two probes (located at 150 and 350 mm) continue to provide reasonable data. A similar situation exists between the probes located at 350 and 500 mm at 0.375 ms. These overlapping data points increase the confidence in the analysis for the inferred current. The inferred current was fit to an exponential waveform, characterized by a peak current at muzzle exit and a time constant for the decay as indicated in Fig. 7. For the three shots conducted the average current at muzzle exit I_o was 88 kA, and the time constant τ was 0.235 ms. The peak current at exit is related to the peak in-bore current and subsequent diffusion. The time constant is related to the conductivity and geometry of the armature and sabot. The variability in I_o and τ for these tests is rather small: less than 10%.

The force tending to clamp the armature halves can be calculated by assuming that two filaments, located in each half of the armature, carry one-half the inferred current. The sabot separates in the rail plane, and the armature is 17 mm thick in the insulator plane. Because the tendency for a transient magnetic field is to reside on the exterior surface of the conductors, the assumption is made that the two loops are separated by a distance p of 17 mm. The force on a current carrying conductor can be calculated from the Lorentz equation:

$$\boldsymbol{F} = \oint I \, \mathrm{d}\boldsymbol{l} \times \mu_o \boldsymbol{H} \tag{4}$$

The EM force tending to clamp the armature halves together can be calculated from the integral

$$F_{\mathrm{EM}} = \int_{b/2}^{-b/2} \mu_o H_x \, \mathrm{d}y \Bigg|_{x=-a/2}^{x=a/2} + \int_{a/2}^{-a/2} \mu_o H_y \, \mathrm{d}x \Bigg|_{y=b/2}^{y=-b/2} \tag{5}$$

Solving with the limits yields the clamping force

$$F_{\mathrm{EM}} = (\mu_o p/\pi)(I/2)^2[-B/p^2 + T/(a^2 + p^2) + T/(b^2 + p^2) - A/p^2] \tag{6}$$

with the following relationships: $T = \sqrt{(a^2 + b^2 + p^2)}$, $B = \sqrt{(b^2 + p^2)}$, and $A = \sqrt{(a^2 + p^2)}$. A plot of F_{EM} as a function of time for Shot 28 is shown in Fig. 8. The force acting on the sabot petals, although very large at muzzle exit, has decayed three orders of magnitude by 1 ms. At a velocity of 1100 m/s, the armature has traveled 1.1 m downrange.

The displacement of the armature petals away from the body of the rod projectile was measured as a function of downrange location. A number of measurement techniques were used and include

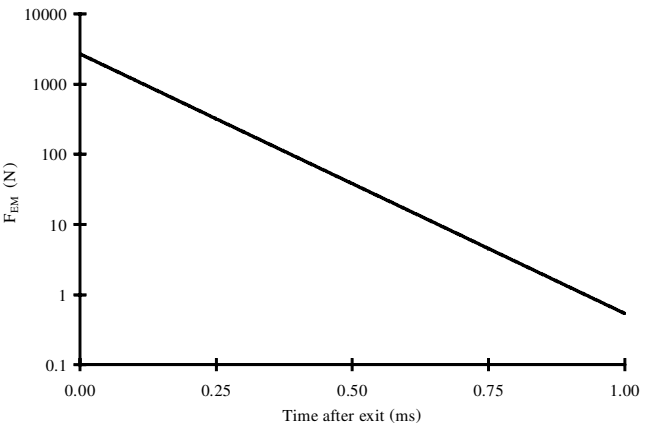

Fig. 8 Magnetic clamping force for shot 28.

an orthogonal x-ray station located at 2.38 m, an orthogonal smear camera located at 4.55 m, and two yaw cards located at 6 and 8 m. From the x-ray image, the armature is still in mechanical contact with the subprojectile, and it is likely that the flowfields from the subprojectile and armature are interacting. From the smear image, the front of the armature has moved significantly off the body of the subprojectile. It is likely that the armature is no longer in aerodynamic contact with the subprojectile. Thus, sabot discard is initiated in the range of 2.38 to 4.55 m.

The trajectory of the sabot was obtained from a simple linear regression of the lateral displacement of the armature from the body of the rod. The location of discard initiation is taken to be the downrange location where the straight-line fit extrapolates to zero petal displacement. The discard is initiated approximately 4 m downrange.

Sabot Discard Model

A simple engineering model was developed to examine the sabot discard process. The purpose of the model was to examine qualitatively the aeromechanics and dynamics of the sabot discard process. The intent of this model is not to demonstrate a validated predictive capability for the sabot discard event but rather to examine whether the observed data are plausible for the present launch package. The model includes the magnetic clamping force in order to determine whether the delayed sabot discard could be attributed to F_{EM} or aerodynamic effects alone.

The sabot petals are designed to provide aerodynamic lifting forces that will cause the sabot petals to separate following launch. The petals have scoops on the forward facing surfaces, which produce an aerodynamic force that cause the sabot petals to lift away early in the sabot separation process. This aerodynamic force is produced by the high-speed external flow that stagnates in the scoops, resulting in a high pressure that will separate the front edge of the two sabot petals. The pressure applied to the scoop surfaces was determined from the stagnation pressure behind a normal shock wave[10] with an upstream Mach number equivalent to the launch Mach number. The net aerodynamic force and moment were evaluated by integrating the pressure over the internal area of the scoops. The analysis includes only the vertical component of the pocket force. The horizontal area of the each scoop A_{pocket} is multiplied by a factor of two to account for the two scoops on each sabot petal:

$$F_{\mathrm{pocket}} = 2A_{\mathrm{pocket}}\left(P_{t_2} - P_2\right), \qquad P_2 = P_\infty \left(1 + \frac{2\gamma}{\gamma + 1}\left(M_\infty^2 - 1\right)\right)$$

$$P_{t_2} = P_2 \left\{1 + \frac{[(\gamma - 1)/2]M_\infty^2 + 1}{[2\gamma/(\gamma - 1)]M_\infty^2 - 1}\right\}^{\gamma/(\gamma - 1)} \tag{7}$$

The sabot petals also provide aerodynamic lift when they are oriented at an angle θ to the oncoming flow. The aerodynamic normal

force was modeled using the force acting on a flat plate in supersonic flow[10]:

$$F_{\text{aero}} = \tfrac{1}{2}\gamma P_\infty M_\infty^2 S\left(4\theta \sqrt{M_\infty^2 - 1}\right) \tag{8}$$

The effective area S for the normal force was taken as the planform area of the sabot petal, and the force was applied at the centroid of this area. This model is clearly an approximation for the actual lift force because aerodynamic effects produced by the complex geometry, petal-to-petal interactions, and high AoA are not considered.

The clamping force attributable to the residual current in the launch package produces a force that resists the opening of the sabot petals. The modeling of this force is described in the preceding section. Finally, as the sabot petals separate, it is possible that there may be some mechanical contact at the rear of the petal as the petals rotate away from the subprojectile. If the sabot discard is symmetrical, the sabot petals produce reaction forces that act against each other. A free-body diagram of forces acting on the sabot petal is shown in Fig. 9.

The equations of motion for the sabot discard are shown next. The moment equation is obtained by summing moments about the rear of the sabot, which allows the reaction force from the interaction of the sabot petals to be eliminated because the reaction force produces zero moment about this point:

$$I_t \ddot{\theta} = F_{\text{aero}} l_{\text{aero}} + F_{\text{pocket}} l_{\text{pocket}} - F_{\text{EM}} l_{\text{EM}} \tag{9}$$

$$m\ddot{x} = (-F_{\text{aero}} - F_{\text{pocket}} + F_{\text{EM}})\sin\theta + F_{x\text{-react}} \tag{10}$$

$$m\ddot{z} = (F_{\text{aero}} + F_{\text{pocket}} - F_{\text{EM}})\cos\theta + F_{z\text{-react}} \tag{11}$$

A summary of the measured physical characteristics of an individual sabot petal is listed in Table 1.

When the sabot petals are in contact, their motion can be determined from the angular motion. The force equations can then be used to determine the x and z components of the reaction force. For the sabot to remain in contact, the reaction force $F_{z\text{-react}}$ must be positive. When $F_{z\text{-react}}$ becomes zero, the rear of the sabot petals will begin to break contact. In this case, the force equations are used to determine the motion of the c.g.

The moment produced by the pocket force is constant throughout the discard process. The moment attributable to the aerodynamic lift force is proportional to the liftoff angle θ, which is initially zero. The magnetic clamping force produces a moment that is assumed to act through the center of the armature body and decays throughout the discard process. The clamping moment is initially much higher than the aerodynamic separation moments. Because the clamping moment in the sabot petal is resisted by an equal but

Table 1 Sabot petal physical parameters

Parameter	Value
Petal mass, m, g	46.8
Moment of inerita, I_t, g-cm^2	298
c.g. from tail, mm	76.15
Petal length, mm	124.4
Pocket width, mm	7
Pocket depth, mm	10
Lifting surface area, mm^2	2613

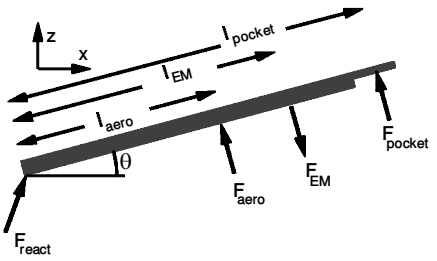

Fig. 9 Free-body diagram of the forces acting on the sabot during discard.

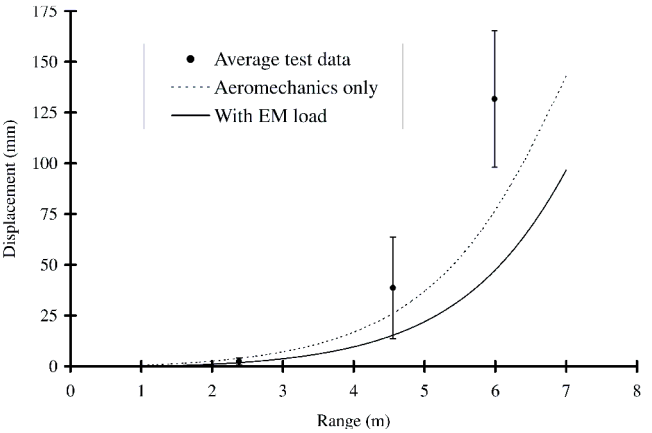

Fig. 10 Displacement of the forward edge of the sabot petal from the outer diameter of the subprojectile rod.

opposite moment from the adjacent sabot petal, the primary effect of the clamping moment shortly after launch is to prevent the sabot petals from separating. The clamping moment continuously decreases because of the exponential decay of the current and eventually becomes smaller than the aerodynamic moment. At this point the petals begin to separate. The moment attributable to the aerodynamic lift is quite small early in the discard process. After 2 m from the muzzle ($\theta = 1$ deg), when the residual current in the armature has decayed substantially, this moment begins to dominate the sabot discard process. At this point, the clamping moment is several orders of magnitude less than the aerodynamic moments and no longer has a significant effect on the sabot discard process. Although reducing the moment arm associated with the clamping force does allow slightly earlier sabot separation, the effect is relatively minor for the current launch package because the clamping moment is initially so large that a significant time is still required to reduce the clamping moment below the aerodynamic moments.

Figure 10 shows a comparison of the predicted lateral displacement of the forward edge of the sabot petal from the outer diameter of the subprojectile rod with the measured displacement from the test matrix. The solid line indicates the calculation with the magnetic clamping force, and the dashed line shows the result with the magnetic clamping force set to zero. The predictions show that when the magnetic clamping force is included the initiation of the sabot discard is delayed by 0.6 m. The computation generally underpredicts the opening of the sabot petals compared with the test data. The agreement between experiment and computation is better earlier in the discard process (first and second measurement stations) where the sabot petal is at less than 10 deg AoA. By the third measurement station, the predicted results indicate the sabot is at 40 deg AoA. The current analysis does not properly account for high AoA, nonlinear lift characteristics of the sabot petals, which may account for some of the differences between predictions and experiment. The analysis indicates that the aerodynamic forces and moments play a significant role in the delayed sabot separation of the present design. The results also show that the clamping force is significant as the predictions indicate an observable change in the discard behavior because of its presence.

Although the data presented in Fig. 10 indicate that the EM clamping force produces a delay in the initiation of sabot discard, the sensitivity of the present analysis should be considered. The model was evaluated over a wide range of values of I_o and τ. Figure 11 shows the increase in range required to achieve the same petal separation relative to the case where only aeromechanical forces are included. The increase in range is expressed as a percentage, and results are presented as a function of I_o for a range of values of τ. Also displayed in the plot is the predicted increase in range for the armature design used in the experiment ($I_o = 88$ kA, $\tau = 235$ μs), where I_o and τ are derived from the analysis of the measured magnetic field data. The plot shows that, although there is a readily measurable effect in the increase in range, for peak exit currents greater than 100 kA the relative increase in range is rather minor. The analysis

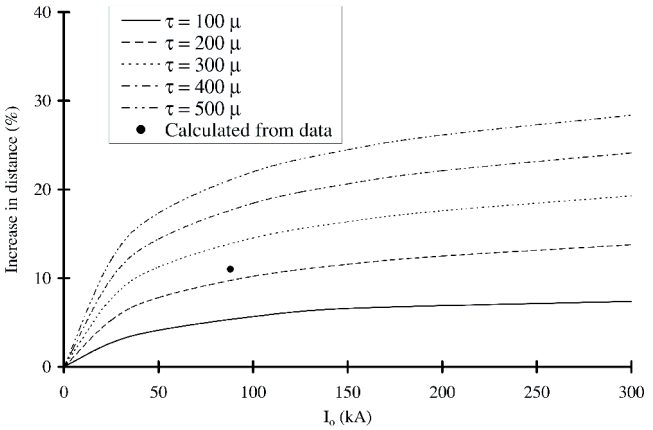

Fig. 11 Percentage change in range required to produce fixed sabot petal separation for various values of I_o and τ.

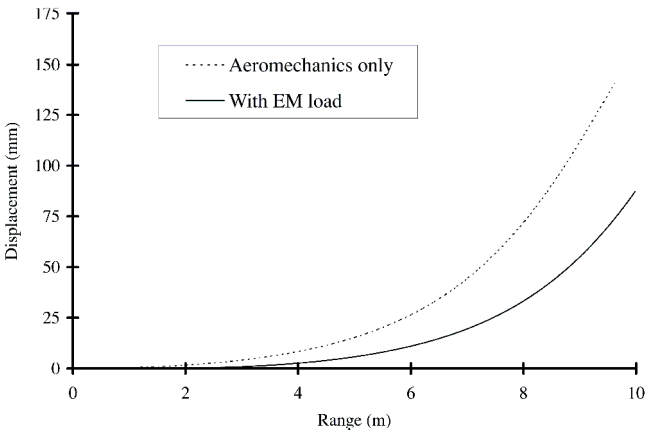

Fig. 12 Calculated sabot discard trajectory for hypervelocity launch.

used to derive I_o and τ can tolerate much larger errors than those referred to in the preceding section without any significant changes in the conclusions regarding sabot discard. Furthermore, the plot also shows that for I_o greater than 100 kA significant changes in the initiation of the petal separation can only be achieved by adjusting τ. The results suggest that τ is an important design parameter in the control of sabot discard from an EM gun. In this analysis, with the exception of one measured data point, the effect of τ has been treated parametrically. To effect a change in τ for a particular application, the armature geometry and materials must be carefully considered. The time constant τ can be determined experimentally (as in the current work) or from computations that consider armature material and geometry. However, such computations are beyond the scope of the current work.

It is useful to consider the effect of hypervelocity launch on the sabot discard trajectory. A peak current of 950 kA was estimated[6] to drive the 140-g launch package to 2500 m/s. The armature current at exit I_o was calculated from the inferred current presented in the preceding section and scaled by the ratio of the peak in-bore currents. This new inferred current (185 kA) is used to calculate F_{EM}. Because the same launch package was assumed for this analysis, the time constant for the decay of the current in the armature was not changed (τ =0.235 ms). The results of the armature trajectory with and without the magnetic clamping force are shown in Fig. 12.

The results indicate that for hypervelocity launch of the present design the sabot discard is expected to occur roughly 30% farther from the muzzle of the gun when compared with the launch velocities used in the current experiments. In the absence of an EM clamping force, retarded separation is expected because the aerodynamic force coefficients decrease somewhat from typical conventional gun velocities to hypervelocity. The clamping force at hypervelocity also produces two effects that retard the sabot separation. First, as modeled here, the time constant associated with the exponential decay of the current is independent of velocity. Thus, the launch package flying at hypervelocity will travel farther before the clamping moments are reduced to the point that the aerodynamic moments can separate the sabot petals. Secondly, the clamping force itself is larger because of the increased current required for launch at 2500 m/s.

Conclusion

Data analysis and measurement techniques were developed and used to assess the effect of electrodynamics on sabot discard. The measurement techniques used in this investigation allow for quick and efficient screening for potentially adverse effects on subprojectile ballistic performance.

The test data and model for sabot discard indicate that the electrodynamics associated with a railgun affect sabot discard. On the basis of magnetic field measurements made within the first 0.5 m downrange from the muzzle, the results indicate that the magnetic field within the armature is negligible after 0.7 m. Sabot discard initiation for this launcher occurs at 4 m downrange from the muzzle. However, the results from the simulation indicate that the magnetic clamping force may preclude discard from initiating earlier in the flight. Two parameters (I_o and τ) were identified that may be useful in minimizing the impact of EM launch on sabot discard. For a launch velocity of 2500 m/s, analysis indicates that the magnetic clamping can delay the initiation of sabot discard. Even without the effect of the magnetic field at hypervelocity, the initiation of sabot discard occurred farther downrange as compared to the low-velocity results.

The power supply used in these experiments forced the armature transport current at exit to near zero. The magnetic field remains trapped in the armature conductor after exit, and circulating currents persist. The present state of the art in pulsed power for EM launchers takes advantage of a zero current at exit because it is advantageous for increased system efficiency. In addition, a zero current at exit can offer reduced launcher signature, blast, and erosion. However, it appears that forcing the armature current to zero at the muzzle does not eliminate the effect of the EM force tending to restrain the sabot petals.

The model revealed several unique features of the sabot discard process. First, EM clamping forces and moments are initially much larger than the aerodynamic forces and moments after launch. The EM forces decay exponentially, and eventually the aerodynamic forces cause the sabot petals to separate. However, the model also showed that the aeromechanical forces considered in the present experimental configuration contribute significantly to the observed delay in sabot discard initiation. The predicted trend of the armature displacement is consistent with the measured data particularly during the early phases of sabot discard. Improved modeling of the aerodynamic lifting force, particularly when the sabot petals are at high incidence, should improve agreement with the measured data later in the sabot discard event. However, these aerodynamic forces have little influence when the EM forces are significant. Application of the model to other velocity regimes and/or geometries is cautioned without further measurements to support the assumptions.

The armature design used in this investigation did not appear to carry any current in the conducting front contact. Other launcher and armature designs may be fabricated to take advantage of the distributed nature of current and forces in the armature. This, in turn, may further diminish the role of the residual magnetic field.

Acknowledgments

Funding for this effort was provided through the Electric Armaments Program Manager, U.S. Army Research Laboratory. We would like to thank Ken Paxton and Barry Hudler for experimental support. We would like to thank Calvin Le (U.S. Army Research Laboratory) for calibrating the magnetic field sensors. Also, very helpful discussions in the area of ballistic performance were held with Peter Plostins and Ed Schmidt. Ameer Mikhail is acknowledged for providing preliminary engineering computations of the sabot discard event.

References

[1]Powell, J. D., and Zielinski, A. E., "Current and Heat Transport in the Solid Armature Railgun," *IEEE Transactions on Magnetics*, Vol. 31, No. 1, 1995, pp. 645–650.

[2]Seiler, S., Legner, H. H., Miller, M., and Reinecke, W. G., "Intermediate Ballistics Model for Hypervelocity Projectiles Launched from EM Guns," *Proceedings of the 15th International Symposium on Ballistics*, Vol. 3, National Defence Research Establishment, Tel Aviv, Israel, 1995, pp. 291–298.

[3]Zielinski, A. E., Weinacht, P., Webb, D. W., and Soencksen, K. P., "An Investigation of the Ballistic Performance for an Electromagnetic Gun-launched Projectile," U.S. Army Research Lab., ARL-TR-1361, Aberdeen Proving Ground, MD, June 1997.

[4]Zielinski, A. E., and Weinacht, P., "Effect of Railgun Electrodynamics on Projectile Launch Dynamics," *IEEE Transactions on Magnetics*, Vol. 35, No. 1, 1999, pp. 118–123.

[5]Zielinski, A. E., and Werst, M., "Cannon-Caliber Electromagnetic Launcher," *IEEE Transactions on Magnetics*, Vol. 33, No. 1, 1997, pp. 630–635.

[6]Zielinski, A. E., and Hildenbrand, D., "Observation and Simulation of Armature Contact Performance in the Cannon-Caliber Electromagnetic Gun," *IEEE Transactions on Magnetics*, Vol. 33, No. 1, 1997, pp. 157–162.

[7]Price, J. H., and Yun, H. D., "Design and Testing of Integrated Metal Armature Sabots for Launch of Armor Penetrating Projectiles from Electric Guns," *IEEE Transactions on Magnetics*, Vol. 31, No. 1, 1995, pp. 219–224.

[8]Schiff, L. B., and Steger, J. L., "Numerical Simulation of Steady Supersonic Viscous Flow," *AIAA Journal*, Vol. 18, No. 12, 1980, pp. 1421–1430.

[9]Murphy, C. H., "Free Flight Motion of Symmetric Missiles," U.S. Army Ballistic Research Lab., Rept. 1216, Aberdeen Proving Ground, MD, July 1963.

[10]John, J. E. A., *Gas Dynamics*, Allyn and Bacon, Boston, 1969, pp. 45, 62, 63, 280–286.

A. C. Tribble
Associate Editor